Geophysical Research Letters

RESEARCH LETTER
10.1029/2021GL093619

Key Points:

- Laboratory earthquakes are associated with seismic velocity and amplitude drops in crustal rocks
- Velocity drops are controlled by the stress acting on the fault and degree of damage in the fault wall
- Amplitude drops are partly controlled by the state of stress and partly affected by dissipative (inelastic) phenomena occurring on-fault

Supporting Information:

Supporting Information may be found in the online version of this article.

Correspondence to:

F. Paglialunga,
federica.paglialunga@epfl.ch

Citation:

Paglialunga, F., Passelègue, F. X., Acosta, M., & Violay, M. (2021). Origin of the co-seismic variations of elastic properties in the crust: Insight from the laboratory. *Geophysical Research Letters*, *48*, e2021GL093619. https://doi.org/10.1029/2021GL093619

Received 1 APR 2021
Accepted 21 MAY 2021

Origin of the Co-Seismic Variations of Elastic Properties in the Crust: Insight From the Laboratory

F. Paglialunga[1], F. X. Passelègue[1], M. Acosta[1], and M. Violay[1]

[1]École Polytechnique Fédérale de Lausanne, LEMR, Lausanne, Switzerland

Abstract Seismological observations highlighted that earthquakes are often followed by changes in elastic properties around the fault zone. Here, we studied the origin of these variations using stick-slip experiments on saw-cut granite samples presenting different degrees of bulk damage (i.e., microcracks). Stick-slip events were induced under triaxial compression configuration with continuous active ultrasonic measurements at confining pressures representative of upper crustal conditions (15–120 MPa). Both the P-wave velocity (V_P) and amplitude (A_P) showed drops, concurrently with stress drops, and had a non-monotonic dependence toward the fault's stress state. Our experimental results suggest that co-seismic changes in V_P were mostly controlled by the elastic re-opening of microcracks in the bulk, rather than by co-seismic damage or the formation of fault gouge. Co-seismic changes in A_P were controlled by a combination of elastic re-opening of microcracks in the bulk and inelastic processes (i.e., co-seismic damage and gouge formation and dilation).

Plain Language Summary Seismological studies have shown that the elastic properties of fault cores can be drastically affected by earthquakes. Despite the large number of studies, the origin of these variations is still debated. It is well known that in the upper crust, faults are surrounded by a zone of damage which could, as well, influence co-seismic changes in elastic properties. We experimentally investigated the influence of a zone of damage surrounding the fault, on the evolution of elastic wave velocity and amplitude during stick-slip experiments (proxies for earthquakes) on thermally treated granite samples. Our results indicate that the presence of a damage zone strongly contributes to the observed changes in elastic properties during earthquakes.

1. Introduction

It is known that during the failure of intact rock specimens, the formation and propagation of microcracks in the bulk increases up to failure, inducing a continuous reduction in seismic velocity (Lockner et al., 1977). If this behavior reflected the failure of natural faults, monitoring the evolution of seismic velocity could help in detecting possible earthquake preparation phases. Earthquakes, effectively, correspond to the brittle failure of the upper crust due to, in the majority of cases, stress accumulation along crustal faults resulting from long-term tectonic loading. Seismological observations highlighted that earthquakes are associated with co-seismic changes in elastic properties around the fault zone (Brenguier et al., 2008; Chen et al., 2010; Froment et al., 2013; Hobiger et al., 2012; Qiu et al., 2020; Wegler et al., 2009; Wu et al., 2016). Most of these studies showed co-seismic velocity variations occurring predominantly in the shallow part of the crust (4–5 km depth). The attributed origin is not unique, and could involve different physical models (Rubinstein & Beroza, 2004): (a) co-seismic damage caused by ground motion, (b) pore pressure variations, (c) microcracks response to static stress change, or (d) fault damage zone response to fault motion. Indeed, in the upper crust, faults are composed by a fault core, where most of the slip occurs, and by a zone of damage surrounding the fault core (Caine et al., 1996; Faulkner et al., 2010; Lockner et al., 2009; Rempe et al., 2013; Wallace & Morris, 1986). While we can have access to direct measurements of the damage zone's width close to the surface (ranging in between few meters and few kilometers), we do not have direct measurements of its evolution with depth, apart from specific drilling projects, which highlight that both the damage zone and fault core are very narrow at depth (Holdsworth et al., 2011). Such observations are supported by a recent numerical study (Okubo et al., 2019), highlighting that the size of the damage zone generated by earthquake ruptures is maximum close to the surface and decreases with depth. Because of that, the

response of fault zones to loading in terms of seismic properties is expected to vary spatially and temporally, and to be a function of both fault structure and travel paths of the seismic waves (Nishizawa, 1982).

To get insights on co-seismic seismic properties variations throughout the seismic cycle, several experimental studies focused at monitoring the evolution of elastic properties through laboratory friction experiments on artificial faults (Kendall & Tabor, 1971). Yoshioka and Iwasa (2006) already used transmission waves to monitor a brass fault contact evolution under normal and shear stress, finding a clear increase in wave amplitude with the increase of normal and shear stresses and amplitude variations linked with precursory slip due to change of the fault's contact area. Following studies performed with gouge interfaces (Kaproth & Marone, 2013; Scuderi et al., 2016; Tinti et al., 2016) showed both co-seismic and precursory changes in P-wave velocity associated with laboratory earthquakes, attributed to the gouge layer dilation and its change of porosity. Scuderi et al. (2016) explored the complete spectrum of failure modes, from slow to fast earthquakes, showing that not only co-seismic changes but also precursory variations of P-wave velocity occur for each mode of failure. Fukuyama et al. (2018) studied amplitude variation during high-velocity friction experiments. Moreover, Shreedharan et al. (2021) showed clear precursory P-wave amplitude variations occurring with the instability nucleation phase and precursory P-wave velocity variations distorted by the presence of the surrounding bulk material. These observations suggest that the elastic properties of the bulk material surrounding the fault may play a role in seismic velocity drops associated to natural earthquakes, as well as its recovery in the months following the rupture. Indeed, seismic waves velocities are sensitive to a change in the degree of damage (i.e., presence of microcracks) of the medium they travel through (Blake et al., 2013; Brantut, 2015; Griffiths et al., 2018; Guéguen & Palciauskas, 1994; Kuttruff, 2012; Nasseri et al., 2009; Nishizawa, 1982).

Our study aims at understanding how much of the change in seismic properties observed during earthquakes is controlled by co-seismic damage occurring on- (i.e., gouge production) and off- (i.e., formation of microcracks in the fault wall due to seismic rupture) fault, and how much is instead affected by the presence of the initial degree of damage characterizing the bulk material and its response to stress changes. To this end, we conducted stick-slip experiments (Brace & Byerlee, 1966) under a wide range of confining pressures on granite saw-cut cylindrical samples presenting two different degrees of initial bulk damage, to mimic different fault damage zone properties.

2. Experimental Methods

2.1. Materials

The tested material is La Peyratte granite, a crustal rock presenting a modal composition of 38.5% plagioclase, 28.5% quartz, 20% K-Feldspar, 13% biotite with an average grain size of 800 μm.

Right-circular cylindrical samples were prepared with 38 mm diameter and 78 mm height. Some were thermally treated before the experiments by slowly heating them (5°C/min, to avoid thermal gradients inside the sample (Wang et al., 2013)) up to different target temperatures (650°C) and let cool down to ambient temperature inside the oven overnight, to avoid thermal shock. Target temperatures were chosen above the α-β quartz transition (572°C), allowing intense intra-granular cracking, randomly oriented in the bulk, producing isotropically damaged media (Glover et al., 1995; Pimienta et al., 2019; Wang et al., 2013), with reduced fracture toughness (Kang et al., 2020; Nasseri et al., 2007). To characterize the different samples, density and porosity were measured, obtaining densities of 2.63 g/cm^3 and 2.58 g/cm^3 and porosities of 0.4% and 6.6%, respectively, for non-treated and thermally treated granite at 650°C.

Samples were saw-cut with an orientation of 30° to the vertical axis, creating an artificial fault plane. The fault roughness was imposed by hand using #240 grit sandpaper, generating a smooth fault, optimally oriented for reactivation, avoiding the propagation of new secondary fractures in the surrounding medium (Renard et al., 2020). The lack of secondary fracture formation under this configuration has been verified in previous experimental work (e.g., Acosta et al. [2019]'s supporting information). A strain gauge was glued on the sample at an intermediate distance between the fault and the sample edge, measuring the axial deformation of the bulk material (Figure 1a).

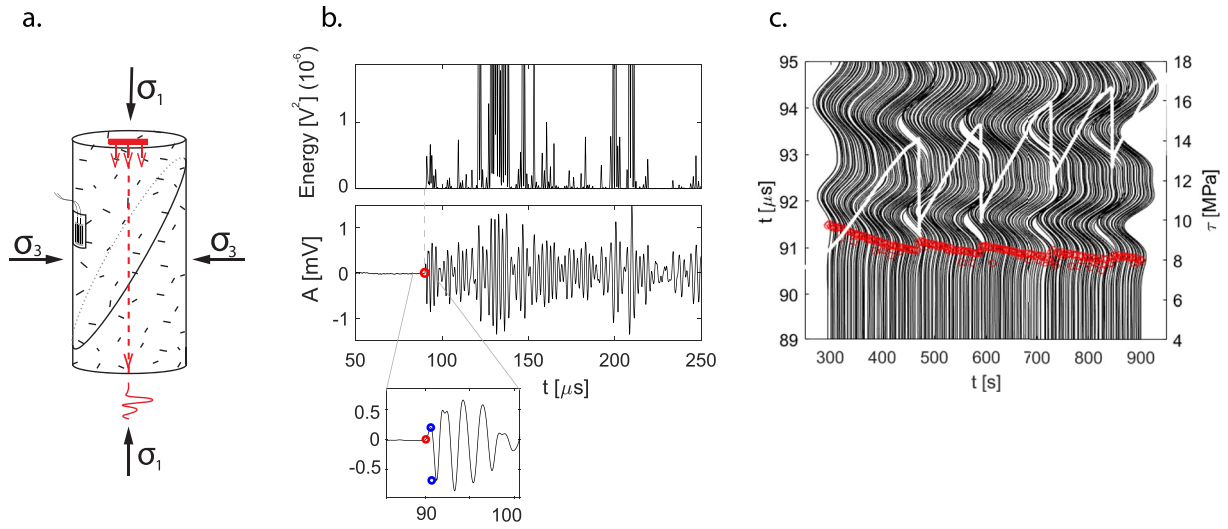

Figure 1. (a) Sample configuration with applied external loads σ_1, σ_3, pulsing direction (in red) and strain gauge location. (b) P-wave arrival time detection; the top panel displays the wave energy evolution with time, the bottom panel displays the detected P-wave arrival time (in red), and P-wave first arrival amplitude (inset, in blue). (c) Seismic waves evolution during a stick-slips series performed for a treated sample at a P_C of 15 MPa. Red markers indicate the arrival time detected by the automatic picking. Shown waves are sampled (1:5). In white, the shear stress evolution during the test.

2.2. Testing Procedure

Tests were run in an oil medium high-pressure triaxial apparatus, FIRST (installed at LEMR, EPFL). The samples were first submitted to a target confining pressure (P_C) (15, 30, 45, 60, 90, and 120 MPa), with a subsequent increase of axial load. Axial load was applied by controlling the oil flow rate (0.25 or 0.50 ml/min in few cases), pushing the piston, generating a displacement rate of $\sim 6 \cdot 10^{-6}$ mm/s. For the different samples (non-treated and treated), experiments were conducted starting from the lowest P_C and, once the stick-slips series was performed, P_C was increased to the following target P_C and a new stick-slips series performed, up to the highest target P_C. Two displacement transducers were placed beside the sample, measuring locally the sample' shortening and/or the fault slip. Mechanical data were recorded at a frequency of 100 Hz for the whole duration of the tests.

2.3. Acoustic Measurements

Active acoustic measurements were recorded during deformation, using acoustic sensors (PZT crystal) placed inside the top and bottom anvils of the triaxial apparatus, with a recording frequency of 100 Hz. The acquisition system setup and the picking procedure were modified and adapted from Acosta and Violay (2020) (refer to the supporting information for details).

Seismic waveforms were used to measure the evolution of P-wave velocity and amplitude along the experiment. Once detected the P-wave arrival time (t_P) the P-wave velocity (V_P) was computed as

$$V_P = \frac{L_{\text{corrected}}}{t_P} \tag{1}$$

with $L_{\text{corrected}}$ the length of the sample, systematically corrected by the elastic shortening and slip occurring. The P-wave amplitude (A_P) was computed as the difference in amplitude between the first maximum value and minimum value of the P-wave (Figure 1b, inset). Seismic measurements were performed in the vertical direction, parallel to the sample axis (ray path showing the largest variations in wave velocity due to the mechanical anisotropy occurring during differential loading) (refer to the Supporting Information, Figure S1).

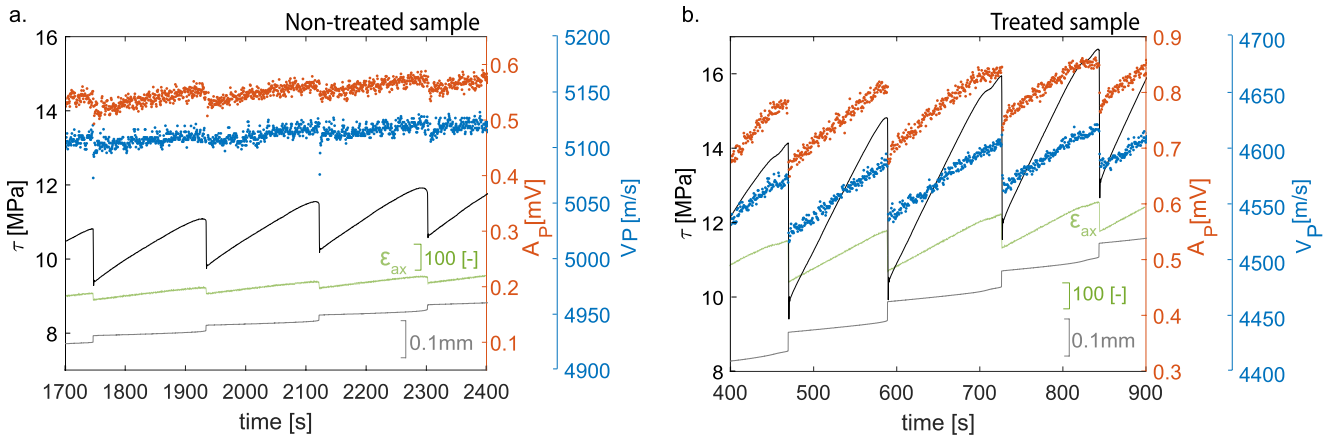

Figure 2. Evolution of shear stress (black), fault slip (gray), axial strain (light green), V_P (blue), and A_P (orange) with time during instabilities at P_C =15 MPa for non-treated (a) and treated sample (b).

3. Experimental Results

Stick-slip experiments conducted under different P_C were used to investigate seismic properties evolution throughout the seismic cycle. For each of them, the shear stress increased first linearly and, once reached the fault strength, dropped to a residual value (Figure 2). As expected, the higher the applied P_C, the higher the fault strength, stress drop, and resulting slip were observed. Concerning the seismic properties, an increase of V_P and A_P was observed during the hydrostatic loading up to the target P_C. Moreover, both V_P and A_P responded to the applied differential stress accordingly, increasing during loading and decreasing during unloading. For both the non-treated and treated sample, the increase in V_P during differential loading ($IV_P^{loading}$) was larger for low P_C, and smaller for high P_C (Figure S2). In particular for the non-treated sample, $IV_P^{loading}$ (from $(\sigma_1 - \sigma_3) = 0$ to the fault's strength) was ~200 m/s, ~140 m/s, ~90 m/s, ~80 m/s, respectively at a P_C of 15, 30, 60, and 90 MPa. For the treated sample, $IV_P^{loading}$ was ~390 m/s, ~220 m/s, ~150 m/s, respectively at a P_C of 15, 45, and 120 MPa. A_P changed in a similar way during differential loading ($IA_P^{loading}$) for the different P_C. $IA_P^{loading}$ for the non-treated sample was $\sim 3.3 \times 10^{-4}$ V, $\sim 1.9 \times 10^{-4}$ V, $\sim 1.0 \times 10^{-4}$ V, respectively at a P_C of 15, 30, 60, and 90 MPa. For the treated sample, $IA_P^{loading}$ was $\sim 4.5 \times 10^{-4}$ V, $\sim 4.55 \times 10^{-4}$ V, and $\sim 1.2 \times 10^{-4}$ V, respectively at a P_C of 15, 45, and 120 MPa. As stress drops occurred, associated to seismic fault slip, a drop in V_P as well as in A_P was observed.

These co-seismic drops in velocity (ΔV_P) and amplitude (ΔA_P) were computed for each stick-slip, and compared with their respective stress conditions (Figure 3). ΔV_P did not show a linear dependence on stress conditions applied to the fault (i.e., normal stress, confining pressure, and shear stress). In the case of non-treated sample, for low P_C (15–30 MPa), hence for low $\Delta\tau$ (~1–3 MPa), ΔV_P were larger (~4–9 m/s) than for events recorded at higher P_C (60 MPa) and medium $\Delta\tau$ (~4–9 MPa), which were ~2–6 m/s. For higher P_C (90 MPa) and the highest $\Delta\tau$ (~12–28 MPa), ΔV_P increased again (~4–9 m/s). The same trend was observed for the treated sample, but with much larger ΔV_P. For low P_C (15 MPa), hence for low $\Delta\tau$ (~3–4 MPa), ΔV_P were larger (~25–50 m/s) than for events recorded at higher P_C (30–45 MPa), hence for medium $\Delta\tau$ (~4–9 MPa), which were ~6–18 m/s. For higher P_C (60–90–120 MPa), and the highest $\Delta\tau$ (~15–45 MPa), ΔV_P increased again (~15–30 m/s). Overall, a large difference in magnitude was noted between the non-treated and the treated sample (Figure 2): the latter showed larger increases during elastic loading and larger drops for similar stress drops. ΔA_P evolution with stress conditions is similar to ΔV_P evolution, with higher values for low P_C and high P_C and lower values for intermediate P_C, for both the non-treated and the treated samples (Figure 3 in color bar).

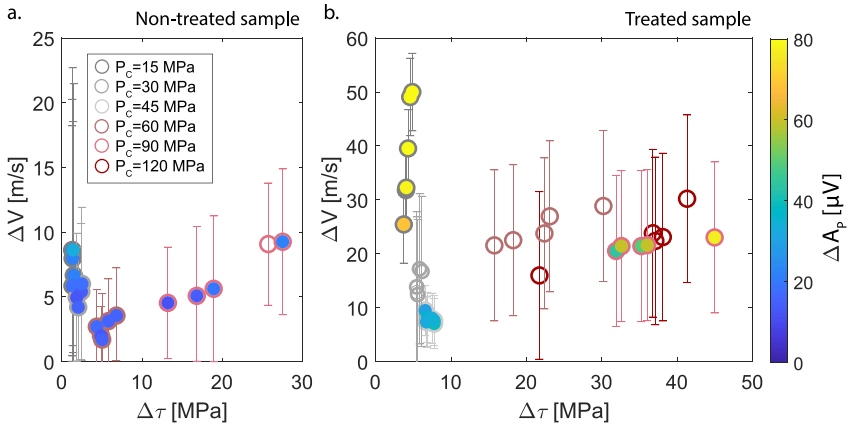

Figure 3. P-wave velocity drops (ΔV_P) evolution with associated shear stress acting on the fault measured during stick-slips for the different P_C for on-treated (a) and treated (b) sample. Error bars indicate the error related to the velocity drop estimation. The observed ΔV_P correspond in percentage to a range of 0.03%–0.35% and 0.16%–1.23%, respectively, for the non-treated and treated sample. Color bar indicates associated P-wave amplitude drops (ΔA_P). Empty symbols are for cases in which it was not possible to measure ΔA_P.

4. Discussion

In our experiments, a non-monotonic ΔV_P evolution with shear stress drops was observed (Figure 3), suggesting that distinct physical processes coexist at the origin of velocity changes during stick-slip instabilities, due to the combination of initial bulk damage and loading conditions. In particular, these drops in velocity during stick-slip events could be related to (i) horizontal microcracks re-opening in the bulk, after initial closure during increasing differential stress (Passelègue et al., 2018), due to differential stress reduction or (ii) co-seismic damage induced around the fault during dynamic rupture propagation and fault motion (Marty et al., 2019; Okubo et al., 2019).

To test these hypotheses, we estimated the maximum possible contribution of microcracks re-opening due to co-seismic stress drop on the associated ΔV_P. Such effect is expected to be similar during both loading and unloading of the bulk (if no adhesion is considered on the microcrack, for example, stress-induced microcrack opening/closure is a reversible process). Under these assumptions, $IV_P^{loading}$ for each P_C can be used to estimate the contribution of microcracks opening following co-seismic stress drops and associated strain release, not considering possible co-seismic damage occurring off-fault. We predicted ΔV_P only due to the re-opening of microcracks occurring in the bulk as follows:

$$\Delta V_P^{predicted} = \frac{\Delta \varepsilon_{ax}}{I\varepsilon_{ax}^{loading}} \cdot IV_P^{loading} \quad (2)$$

where $\Delta\varepsilon_{ax}$ is the drop in axial strain measured concurrently with stress drop, $I\varepsilon_{ax}^{loading}$ the increase in axial strain during differential loading (strain gauge located in the bulk material, far enough from the fault, expected to capture elastic deformation of the bulk).

$\Delta V_P^{predicted}$ for all the events at each Pc for both treated and non-treated samples, showed the same evolution with loading conditions of the ones experimentally observed $\left(\Delta V_P^{measured}\right)$. In fact, by plotting them together (Figure 4a), a linear dependence between the two is noted, with a slope very close to 1:1, indicating that $\Delta V_P^{measured}$ are well explained by the co-seismic re-opening of microcracks in the bulk, resulting from the release of strain. This suggests that in our experimental configuration, no significant co-seismic damage was generated during rupture propagation, or it was negligible with respect to the observed velocity variations. Once again, the non-monotonic trend observed as a function of applied stress (Figure 3) is explained by the interplay between P_C and $IV_P^{loading}$. For low P_C the induced stress drops are very small (~1–3 MPa/~3–4 MPa, respectively, for non-treated and treated sample) but the related $IV_P^{loading}$ (seen here as the maximum potential velocity drop caused by microcracks opening, at a specific P_C) is very large (~200/~390 m/s), generating

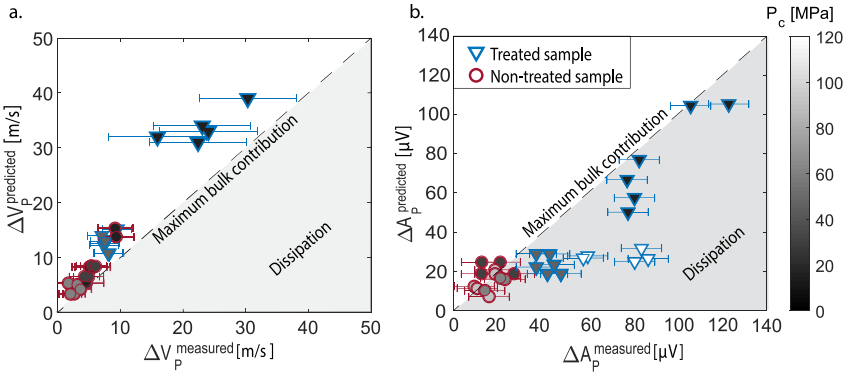

Figure 4. (a) $\Delta V_P^{predicted}$ vs. $\Delta V_P^{measured}$ are shown for non-treated (in burgundy) and treated (in blue) samples. The dashed line represents the 1:1 slope which divides the plot in two regions: (in white) domain where ΔV_P are completely explained by elastic re-opening of the microcracks present in the bulk (in gray) dissipative domain, where ΔV_P are explained by dissipative phenomena like co-seismic damage and gouge shearing. (b) $\Delta A_P^{predicted}$ vs $\cdot \Delta A_P^{measured}$ are shown for non-treated (in burgundy) and treated (in blue) samples. The black line divides the plot in two regions: (in white) domain where ΔA_P are completely explained by elastic re-opening of the microcracks present in the bulk (in gray) dissipative domain, where ΔA_P are explained by dissipative (inelastic) phenomena (i.e., shearing of the gouge layer).

high velocity drops (~4–9/~7–50 m/s). On the contrary, for medium P_C the induced stress drops are a bit higher (~4–9 MPa), but the corresponding $IV_P^{loading}$ is lower (~140/~210 m/s), generating quite small velocity drops (~2–6/~6–18 m/s), while for high P_C the observed stress drops are very large (~12–28/~15–45 MPa) and even if the related $IV_P^{loading}$ is very small (~80 m/s/~150 m/s), the resulting velocity drops are larger (~4–9/~15–30 m/s) (refer to Supporting Information and Figure S4 for a conceptual scheme).

Remarkably, while co-seismic ΔV_P proved, in our experiments, to be mostly related to the re-opening of microcracks in the bulk and elastic relaxation, we could observe some gouge production on the post mortem samples fault surfaces (in particular on the one of the treated sample), which is expected to have an influence on the seismic properties measured across the sample (Scuderi et al., 2016; Shreedharan et al., 2021; Tinti et al., 2016). In particular, the presence of a gouge layer is expected to affect A_P, considered as a simplified way to account for attenuation (Lockner et al., 1977) (i.e., the higher the amplitude of the wave, the lower the attenuation and vice versa). Compared to V_P, which is mainly affected by elastic processes such as microcracks closure and re-opening, A_P is also influenced by the fault's specific stiffness and by the inelastic, dissipative deformation processes occurring on and off-fault (i.e., frictional sliding of microcracks in the bulk and/or gouge particle shearing).

A prediction similar to the one described above (Equation 2) was tempted to test if A_P measured in these experiments was also mainly influenced by the bulk properties and stress conditions. Equation 2 was modified and V_P was replaced by A_P as follows:

$$\Delta A_P^{predicted} = \frac{\Delta \varepsilon_{ax}}{I\varepsilon_{ax}^{loading}} \cdot IA_P^{loading} \quad (3)$$

with $\Delta A_P^{predicted}$ the predicted amplitude drops and $IA_P^{loading}$ the overall increase of A_P during differential loading. For the non-treated sample, the prediction works well, with values falling very close to the prediction line of slope 1:1 (Figure 4b). However, for the treated sample, this is true only for the lower P_C (15 MPa). For higher P_C (45 and 120 MPa), the predicted drops do not mimic the measured ones, the latter being notably larger (up to 400% larger). This might be explained by the change in the fault's contacts and/or by non-elastic processes occurring either in the bulk (i.e., friction caused by shear along microcracks) or on the fault surfaces (i.e., gouge production, shearing, and dilation). Since the expected stress responsible for microcracks shearing is larger than the one expected to activate shearing along the artificial fault, we assume that the non-elastic processes observed are caused by the fault's response to stick-slips. This was verified by analyzing the evolution of A_P with cumulative slip (Figure S3), since (a) gouge production is expected to increase linearly with cumulative fault slip (Archard, 1953) and (b) slip requires shearing of gouge particles

under high applied stresses. Given that (a) the thermally treated sample is expected to have a lower fracture toughness than the non-treated one (Nasseri et al., 2007), (b) we observed a decrease in A_P for consecutive stick-slips only under medium to high P_C (i.e., normal load acting on the fault), and (c) that we could observe a large amount of gouge on the post-mortem sample's fault, we ascribed A_P behavior to be a function of the gouge production (Frérot et al., 2018) and subsequent gouge particles shearing during fault's slip under these conditions. This looks coherent with the evolution of the fault specific stiffness (Pyrak-Nolte et al., 1990) for the different stress conditions (Figure S5), which in the case of the treated sample reaches a sort of saturation for the highest P_C (120 MPa)(i.e., the gouge once filled all the voids available in the interface and compacted, will not deform any further for higher P_C, not influencing k_F).

5. Implications and Conclusions

Summarizing our interpretation of the results, co-seismic ΔV_P seem to be controlled by the combination of bulk properties and applied stress (i.e., re-opening of the microcracks present in the bulk concurrently with stress drop). This does not imply that other phenomena occurring during stick-slips, such as gouge layer dilation, could not contribute to ΔV_P itself, but only that their influence, compared to one of the pre-existing microcracks in the bulk, resulted negligible in our experiments. In addition, while co-seismic ΔA_P also looked to be controlled by the combination of bulk properties and applied stress when the presence of gouge was not dominant, they were probably controlled by dissipative processes occurring on-fault when the conditions (treated sample and higher applied stress) allowed an important production of gouge, hence a necessary shearing of gouge particles.

Conversely to previous experimental studies (Kaproth & Marone, 2013; Scuderi et al., 2016; Shreedharan et al., 2021), no significant and clear precursory variation of seismic velocity and amplitude was observed. This might be due to several reasons; among the others, the localized nature of the nucleation phenomenon, known to be the cause of observed pre-seismic slip. Depending on the nucleation patch size, either a low or a high-stress perturbation will be induced in its vicinity. A nucleation patch length significantly smaller than fault length is expected under this configuration (Harbord et al., 2017). Assuming this, the stress release during the nucleation of instability is expected to affect only a small fraction of the whole sample, without inducing any strong premonitory change in V_P or A_P. Another reason could be related to our resolution of the seismic measurements, which may be not high enough to capture precursory changes which remain lost within the error linked to the present measurements.

However, our results could help to better understand in which conditions precursory variations of seismic properties can actually be detected and used to monitor fault's state of stress. It is clear that the wallrock's elastic properties have a huge control on the seismic properties measured across the system. It was recently shown that this distortion is crucial for observations of the aforementioned precursory phase (Shreedharan et al., 2021). For this reason, the luckiest combination to observe this variation would be to encounter a fault composed by a wide gouge layer and with a large nucleation patch. The shearing of gouge particles within the fault zone will strongly affect the seismic amplitude, which is the parameter the most sensitive to inelastic processes.

Moreover, even if a direct comparison remains risky given the differences in the applied conditions and the large uncertainties in the estimation, there are some analogies between the relative variations in V_P recorded in this study and the ones observed after real earthquakes. It emerges that the overall range of values measured in our experiments (0.03%–0.35% and 0.16%–1.23% respectively for non-treated and treated sample), performed under stress conditions representative of the upper crust, is comparable to the ranges of values measured after real earthquakes (Brenguier et al. [2008] estimate variations of ∼0.02%–0.07%, Chen et al. [2010] find ∼0.04%–0.08%, Nimiya et al. [2017] find ∼0.4%–0.8%, Qiu et al. [2020] find ∼0.15%–0.25%, Taylor and Hillers [2020] find ∼0.15%). The similarity between our observations and the ones referring to natural earthquakes, suggests that the monitored seismic properties could be controlled by the same factors (i.e., combination of propagation of seismic waves through fault core, damage zone, wallrock). In fact, measurements performed across artificial gouge faults, monitoring V_P evolution of the only gouge layer with

no contribution of the surrounding medium, showed much higher relative V_P variations ~1%–4% (Scuderi et al., 2016; Tinti et al., 2016) (for a graphical representation refer to the Supporting Information, Figure S8).

Finally, given the impossibility to measure natural seismic variations of the only fault core, monitoring the evolution of seismic velocity along faults surrounded by large damage zones, could be of interest for observing co-seismic changes during shallow earthquakes, since the combination of large and highly damage zones and low-stress conditions lead to an extremely high sensitivity in velocity changes due to stress perturbations, especially at low depths. Moreover, since many earthquakes are preceded by a nucleation stage (Latour et al., 2013; Ohnaka, 2003; Ruiz et al., 2014; Socquet et al., 2017; Tape et al., 2018), which is expected to release part of the stress along the fault, the amplitude evolution may provide, under the aforementioned conditions, some indications about stress evolution along the fault and the proximity to failure. This kind of observations could, yet, be limited by the current spatial resolution of seismological observations and by the knowledge of the damage zones in seismogenic faults.

Data Availability Statement

The raw data can be found at the following address: http://doi.org/10.5281/zenodo.4892328.

Acknowledgments
F.P. and M.V. acknowledge the European Research Council Starting Grant project 757290-BEFINE. F.X.P. acknowledges the Swiss National Science Foundation Grant PZENP2/173613. Authors thank two anonymous reviewers for their constructive comments.

References

Acosta, M., Passelègue, F. X., Schubnel, A., Madariaga, R., & Violay, M. (2019). Can precursory moment release scale with earthquake magnitude? A view from the laboratory. *Geophysical Research Letters*, *46*(22), 12927–12937. https://doi.org/10.1029/2019gl084744

Acosta, M., & Violay, M. (2020). Mechanical and hydraulic transport properties of transverse-isotropic gneiss deformed under deep reservoir stress and pressure conditions. *International Journal of Rock Mechanics and Mining Sciences*, *130*, 104235. https://doi.org/10.1016/j.ijrmms.2020.104235

Archard, J. F. (1953). Contact and rubbing of flat surfaces. *Journal of Applied Physics*, *24*(8), 981–988. https://doi.org/10.1063/1.1721448

Blake, O. O., Faulkner, D. R., & Rietbrock, A. (2013). The effect of varying damage history in crystalline rocks on the P- and S-wave velocity under hydrostatic confining pressure. *Pure and Applied Geophysics*, *170*(4), 493–505. https://doi.org/10.1007/s00024-012-0550-0

Brace, W. F., & Byerlee, J. D. (1966). Stick-slip as a mechanism for earthquakes. *Science*, *153*(3739), 990–992. https://doi.org/10.1126/science.153.3739.990

Brantut, N. (2015). Time-dependent recovery of microcrack damage and seismic wave speeds in deformed limestone. *Journal of Geophysical Research: Solid Earth*, *120*(12), 8088–8109. https://doi.org/10.1002/2015jb012324

Brenguier, F., Campillo, M., Hadziioannou, C., Shapiro, N. M., Nadeau, R. M., & Larose, E. (2008). Postseismic relaxation along the San Andreas Fault at Parkfield from continuous seismological observations. *Science*, *321*(5895), 1478–1481. https://doi.org/10.1126/science.1160943

Caine, J. S., Evans, J. P., & Forster, C. B. (1996). Fault zone architecture and permeability structure. *Geology*, *24*(11), 1025–1028. https://doi.org/10.1130/0091-7613(1996)024<1025:fzaaps>2.3.co;2

Chen, J. H., Froment, B., Liu, Q. Y., & Campillo, M. (2010). Distribution of seismic wave speed changes associated with the 12 May 2008 Mw 7.9 Wenchuan earthquake. *Geophysical Research Letters*, *37*(18). https://doi.org/10.1029/2010gl044582

Faulkner, D. R., Jackson, C. A. L., Lunn, R. J., Schlische, R. W., Shipton, Z. K., Wibberley, C. A. J., & Withjack, M. O. (2010). A review of recent developments concerning the structure, mechanics and fluid flow properties of fault zones. *Journal of Structural Geology*, *32*(11), 1557–1575. https://doi.org/10.1016/j.jsg.2010.06.009

Frérot, L., Aghababaei, R., & Molinari, J. F. (2018). A mechanistic understanding of the wear coefficient: From single to multiple asperities contact. *Journal of the Mechanics and Physics of Solids*, *114*, 172–184. https://doi.org/10.1016/j.jmps.2018.02.015

Froment, B., Campillo, M., Chen, J. H., & Liu, Q. Y. (2013). Deformation at depth associated with the 12 May 2008 MW 7.9 Wenchuan earthquake from seismic ambient noise monitoring. *Geophysical Research Letters*, *40*(1), 78–82. https://doi.org/10.1029/2012gl053995

Fukuyama, E., Yamashita, F., & Mizoguchi, K. (2018). Voids and rock friction at subseismic slip velocity. *Pure and Applied Geophysics*, *175*(2), 611–631. https://doi.org/10.1007/s00024-017-1728-2

Glover, P. W. J., Baud, P., Darot, M., Meredith, P. G., Boon, S. A., LeRavalec, M., et al. (1995). α/β phase transition in quartz monitored using acoustic emissions. *Geophysical Journal International*, *120*(3), 775–782. https://doi.org/10.1111/j.1365-246x.1995.tb01852.x

Griffiths, L., Lengliné, O., Heap, M. J., Baud, P., & Schmittbuhl, J. (2018). Thermal cracking in westerly granite monitored using direct wave velocity, coda wave interferometry, and acoustic emissions. *Journal of Geophysical Research: Solid Earth*, *123*(3), 2246–2261. https://doi.org/10.1002/2017jb015191

Guéguen, Y., & Palciauskas, V. (1994). *Introduction to the physics of rocks*. Princeton University Press.

Harbord, C. W. A., Nielsen, S. B., De Paola, N., & Holdsworth, R. E. (2017). Earthquake nucleation on rough faults. *Geology*, *45*(10), 931–934. https://doi.org/10.1130/g39181.1

Hobiger, M., Wegler, U., Shiomi, K., & Nakahara, H. (2012). Coseismic and postseismic elastic wave velocity variations caused by the 2008 Iwate-Miyagi Nairiku earthquake, Japan. *Journal of Geophysical Research: Solid Earth*, *117*, B09313. https://doi.org/10.1029/2012jb009402

Holdsworth, R. E., van Diggelen, E. W. E., Spiers, C. J., de Bresser, J. H. P., Walker, R. J., & Bowen, L. (2011). Fault rocks from the SAFOD core samples: Implications for weakening at shallow depths along the San Andreas Fault, California. *Journal of Structural Geology*, *33*(2), 132–144. https://doi.org/10.1016/j.jsg.2010.11.010

Kang, P., Hong, L., Fazhi, Y., Quanle, Z., Xiao, S., & Zhaopeng, L. (2020). Effects of temperature on mechanical properties of granite under different fracture modes. *Engineering Fracture Mechanics*, *226*, 106838. https://doi.org/10.1016/j.engfracmech.2019.106838

Kaproth, B. M., & Marone, C. (2013). Slow earthquakes, preseismic velocity changes, and the origin of slow frictional stick-slip. *Science*, *341*(6151), 1229–1232. https://doi.org/10.1126/science.1239577

Kendall, K., & Tabor, D. (1971). An ultrasonic study of the area of contact between stationary and sliding surfaces. *Proceedings of the Royal Society of London. A. Mathematical and Physical Sciences*, *323*(1554), 321–340. https://doi.org/10.1098/rspa.1971.0108

Kuttruff, H. (2012). *Ultrasonics: Fundamentals and applications*. Springer Science & Business Media.

Latour, S., Schubnel, A., Nielsen, S., Madariaga, R., & Vinciguerra, S. (2013). Characterization of nucleation during laboratory earthquakes. *Geophysical Research Letters*, *40*(19), 5064–5069. https://doi.org/10.1002/grl.50974

Lockner, D. A., Tanaka, H., Ito, H., Ikeda, R., Omura, K., & Naka, H. (2009). Geometry of the Nojima Fault at Nojima-Hirabayashi, Japan-I. A simple damage structure inferred from borehole core permeability. *Pure and Applied Geophysics*, *166*(10–11), 1649–1667. https://doi.org/10.1007/978-3-0346-0138-2_6

Lockner, D. A., Walsh, J. B., & Byerlee, J. D. (1977). Changes in seismic velocity and attenuation during deformation of granite. *Journal of Geophysical Research*, *82*(33), 5374–5378. https://doi.org/10.1029/jb082i033p05374

Marty, S., Passelègue, F. X., Aubry, J., Bhat, H. S., Schubnel, A., & Madariaga, R. (2019). Origin of high-frequency radiation during laboratory earthquakes. *Geophysical Research Letters*, *46*(7), 3755–3763. https://doi.org/10.1029/2018gl080519

Nasseri, M. H. B., Schubnel, A., Benson, P. M., & Young, R. P. (2009). Common evolution of mechanical and transport properties in thermally cracked westerly granite at elevated hydrostatic pressure. *Pure and Applied Geophysics*, *166*(5–7), 927–948. https://doi.org/10.1007/978-3-0346-0122-1_9

Nasseri, M. H. B., Schubnel, A., & Young, R. P. (2007). Coupled evolutions of fracture toughness and elastic wave velocities at high crack density in thermally treated westerly granite. *International Journal of Rock Mechanics and Mining Sciences*, *44*(4), 601–616. https://doi.org/10.1016/j.ijrmms.2006.09.008

Nimiya, H., Ikeda, T., & Tsuji, T. (2017). Spatial and temporal seismic velocity changes on Kyushu Island during the 2016 Kumamoto earthquake. *Science Advances*, *3*(11). https://doi.org/10.1126/sciadv.1700813

Nishizawa, O. (1982). Seismic velocity anisotropy in a medium containing oriented cracks-transversely isotropic case. *Journal of Physics of the Earth*, *30*(4), 331–347. https://doi.org/10.4294/jpe1952.30.331

Ohnaka, M. (2003). A constitutive scaling law and a unified comprehension for frictional slip failure, shear fracture of intact rock, and earthquake rupture. *Journal of Geophysical Research: Solid Earth*, *108*(B2). https://doi.org/10.1029/2000jb000123

Okubo, K., Bhat, H. S., Rougier, E., Marty, S., Schubnel, A., Lei, Z., et al. (2019). Dynamics, radiation, and overall energy budget of earthquake rupture with coseismic off-fault damage. *Journal of Geophysical Research: Solid Earth*, *124*(11), 11771–11801. https://doi.org/10.1029/2019jb017304

Passelègue, F. X., Lucas Pimienta, D. F., Schubnel, A., Fortin, J., Guéguen, Y., & Guéguen, Y. (2018). Development and recovery of stress-induced elastic anisotropy during cyclic loading experiment on westerly granite. *Geophysical Research Letters*, *45*(16), 8156–8166. https://doi.org/10.1029/2018gl078434

Pimienta, L., Orellana, L. F., & Violay, M. (2019). Variations in elastic and electrical properties of crustal rocks with varying degree of microfracturation. *Journal of Geophysical Research: Solid Earth*, *124*(7), 6376–6396. https://doi.org/10.1029/2019jb017339

Pyrak-Nolte, L. J., Myer, L. R., & Cook, N. G. W. (1990). Transmission of seismic waves across single natural fractures. *Journal of Geophysical Research*, *95*(B6), 8617–8638. https://doi.org/10.1029/jb095ib06p08617

Qiu, H., Hillers, G., & Ben-Zion, Y. (2020). Temporal changes of seismic velocities in the San Jacinto fault zone associated with the 2016 Mw 5.2 Borrego Springs earthquake. *Geophysical Journal International*, *220*(3), 1536–1554. https://doi.org/10.1093/gji/ggz538

Rempe, M., Mitchell, T., Renner, J., Nippress, S., Ben-Zion, Y., & Rockwell, T. (2013). Damage and seismic velocity structure of pulverized rocks near the San Andreas fault. *Journal of Geophysical Research: Solid Earth*, *118*(6), 2813–2831. https://doi.org/10.1002/jgrb.50184

Renard, F., Mcbeck, J., & Cordonnier, B. (2020). Competition between slow slip and damage on and off faults revealed in 4D synchrotron imaging experiments. *Tectonophysics*, *782–783*, 228437. https://doi.org/10.1016/j.tecto.2020.228437

Rubinstein, J. L., & Beroza, G. C. (2004). Evidence for widespread nonlinear strong ground motion in the M_w 6.9 Loma Prieta Earthquake. *Bulletin of the Seismological Society of America*, *94*(5), 1595–1608. https://doi.org/10.1785/012004009

Ruiz, S., Metois, M., Fuenzalida, A., Ruiz, J., Leyton, F., Grandin, R., et al. (2014). Intense foreshocks and a slow slip event preceded the 2014 Iquique Mw 8.1 earthquake. *Science*, *345*(6201), 1165–1169. https://doi.org/10.1126/science.1256074

Scuderi, M. M., Marone, C., Tinti, E., Di Stefano, G., & Collettini, C. (2016). Precursory changes in seismic velocity for the spectrum of earthquake failure modes. *Nature Geoscience*, *9*(9), 695–700. https://doi.org/10.1038/ngeo2775

Shreedharan, S., Bolton, D. C., Rivière, J., Marone, C., & La Sapienza (2021). Competition between preslip and deviatoric stress modulates precursors for laboratory earthquakes. *Earth and Planetary Science Letters*, *553*, 116623. https://doi.org/10.1016/j.epsl.2020.116623

Socquet, A., Valdes, J. P., Jara, J., Cotton, F., Walpersdorf, A., Cotte, N., et al. (2017). An 8 month slow slip event triggers progressive nucleation of the 2014 Chile megathrust. *Geophysical Research Letters*, *44*(9), 4046–4053. https://doi.org/10.1002/2017gl073023

Tape, C., Holtkamp, S., Silwal, V., Hawthorne, J., Kaneko, Y., Paul Ampuero, J., et al. (2018). Earthquake nucleation and fault slip complexity in the lower crust of Central Alaska. *Nature Geoscience*, *11*(7), 536–541. https://doi.org/10.1038/s41561-018-0144-2

Taylor, G., & Hillers, G. (2020). estimating temporal changes in seismic velocity using a Markov chain Monte Carlo approach. *Geophysical Journal International*, *220*(3), 1791–1803. https://doi.org/10.1093/gji/ggz535

Tinti, E., Scuderi, M. M., Scognamiglio, L., Di Stefano, G., Marone, C., & Collettini, C. (2016). On the evolution of elastic properties during laboratory stick-slip experiments spanning the transition from slow slip to dynamic rupture. *Journal of Geophysical Research: Solid Earth*, *121*(12), 8569–8594. https://doi.org/10.1002/2016jb013545

Wallace, R. E., & Morris, H. T. (1986). Characteristics of faults and shear zones in deep mines. *Pure and Applied Geophysics*, *124*(1–2), 107–125. https://doi.org/10.1007/bf00875721

Wang, X.-Q., Schubnel, A., Fortin, J., Guéguen, Y., & Ge, H.-K. (2013). Physical properties and brittle strength of thermally cracked granite under confinement. *Journal of Geophysical Research: Solid Earth*, *118*(12), 6099–6112. https://doi.org/10.1002/2013jb010340

Wegler, U., Nakahara, H., Sens-Schönfelder, C., Korn, M., & Shiomi, K. (2009). Sudden drop of seismic velocity after the 2004 Mw 6.6 Mid-Niigata Earthquake, Japan, observed with passive image interferometry. *Journal of Geophysical Research: Solid Earth*, *114*(B6). https://doi.org/10.1029/2008jb005869

Wu, C., Delorey, A., Brenguier, F., Hadziioannou, C., Daub, E. G., & Johnson, P. (2016). Constraining depth range of S wave velocity decrease after large earthquakes near Parkfield, California. *Geophysical Research Letters*, *43*(12), 6129–6136. https://doi.org/10.1002/2016gl069145

Yoshioka, N., & Iwasa, K. (2006). A laboratory experiment to monitor the contact state of a fault by transmission waves. *Tectonophysics*, *413*(3–4), 221–238. https://doi.org/10.1016/j.tecto.2005.10.035

References From the Supporting Information

Birch, F. (1961). The velocity of compressional waves in rocks to 10 kilobars: 2. *Journal of Geophysical Research*, *66*(7), 2199–2224. https://doi.org/10.1029/jz066i007p02199

Fleming, J. R., & Suh, N. P. (1977). The relationship between crack propagation rates and wear rates. *Wear*, *44*(1), 57–64. https://doi.org/10.1016/0043-1648(77)90084-9

Kern, H. (1978). The effect of high temperature and high confining pressure on compressional wave velocities in quartz-bearing and quartz-free igneous and metamorphic rocks. *Tectonophysics*, *44*(1–4), 185–203. https://doi.org/10.1016/0040-1951(78)90070-7

Scholz, C. H. (1987). Wear and gouge formation in brittle faulting. *Geology*, *15*(6), 493–495. https://doi.org/10.1130/0091-7613(1987)15<493:wagfib>2.0.co;2